A&A, 691, A237 (2024)
https://doi.org/10.1051/0004-6361/202451416

Astronomy & Astrophysics

Microlensing brown-dwarf companions in binaries detected during the 2022 and 2023 seasons

Cheongho Han[1], Ian A. Bond[2], Andrzej Udalski[3], Chung-Uk Lee[4,⋆], Andrew Gould[5,6],
Michael D. Albrow[7], Sun-Ju Chung[4], Kyu-Ha Hwang[4], Youn Kil Jung[4], Yoon-Hyun Ryu[4], Yossi Shvartzvald[8],
In-Gu Shin[9], Jennifer C. Yee[9], Hongjing Yang[10], Weicheng Zang[9,10], Sang-Mok Cha[4,11], Doeon Kim[1],
Dong-Jin Kim[4], Seung-Lee Kim[4], Dong-Joo Lee[4], Yongseok Lee[4,11], Byeong-Gon Park[4], Richard W. Pogge[6]
(The KMTNet Collaboration)
Fumio Abe[12], Ken Bando[13], Richard Barry[14], David P. Bennett[14,15], Aparna Bhattacharya[14,15], Hirosame Fujii[12],
Akihiko Fukui[16,17], Ryusei Hamada[13], Shunya Hamada[13], Naoto Hamasaki[13], Yuki Hirao[18], Stela Ishitani Silva[14,19],
Yoshitaka Itow[12], Rintaro Kirikawa[13], Naoki Koshimoto[13], Yutaka Matsubara[12], Shota Miyazaki[20],
Yasushi Muraki[12], Tutumi Nagai[13], Kansuke Nunota[13], Greg Olmschenk[14], Clément Ranc[21],
Nicholas J. Rattenbury[22], Yuki Satoh[13], Takahiro Sumi[13], Daisuke Suzuki[13], Mio Tomoyoshi[13], Paul J. Tristram[23],
Aikaterini Vandorou[14,15], Hibiki Yama[13], Kansuke Yamashita[13]
(The MOA Collaboration)
Przemek Mróz[3], Michał K. Szymański[3], Jan Skowron[3], Radosław Poleski[3], Igor Soszyński[3],
Paweł Pietrukowicz[3], Szymon Kozłowski[3], Krzysztof A. Rybicki[3,8], Patryk Iwanek[3], Krzysztof Ulaczyk[24],
Marcin Wrona[3,25], Mariusz Gromadzki[3], and Mateusz J. Mróz[3]
(The OGLE Collaboration)

(Affiliations can be found after the references)

Received 7 July 2024 / Accepted 18 August 2024

ABSTRACT

Aims. Building on previous works to construct a homogeneous sample of brown dwarfs in binary systems, we investigate microlensing events detected by the Korea Microlensing Telescope Network (KMTNet) survey during the 2022 and 2023 seasons.

Methods. Given the difficulty in distinguishing brown-dwarf events from those produced by binary lenses with nearly equal-mass components, we analyze all lensing events detected during the seasons that exhibit anomalies characteristic of binary-lens systems.

Results. Using the same criteria consistently applied in previous studies, we identify six additional brown dwarf candidates through the analysis of lensing events KMT-2022-BLG-0412, KMT-2022-BLG-2286, KMT-2023-BLG-0201, KMT-2023-BLG-0601, KMT-2023-BLG-1684, and KMT-2023-BLG-1743. An examination of the mass posteriors shows that the median mass of the lens companions ranges from $0.02\,M_\odot$ to $0.05\,M_\odot$, indicating that these companions fall within the brown-dwarf mass range. The mass of the primary lenses ranges from $0.11\,M_\odot$ to $0.68\,M_\odot$, indicating that they are low-mass stars with substantially lower masses compared to the Sun.

Key words. gravitational lensing: micro

1. Introduction

Brown dwarfs (BDs) are substellar objects capable of undergoing deuterium fusion, yet lacking the mass required for sustaining hydrogen fusion. This places them in a mass range between stars and planets (Burrows et al. 1997; Chabrier & Baraffe 2000). Understanding the binary properties of BDs, such as binary frequency, separation, and mass-ratio distributions, is essential for comprehending these objects as these properties provide insights into both their formation processes and the dynamic interactions within systems. For instance, the scarcity of BDs in close orbits relative to the frequency of either less massive planetary companions or more massive stellar companions, known as the BD desert (Marcy & Butler 2000; Grether & Lineweaver 2006), has been observed around solar-mass stars. This may suggest the possibility of inward migration of BD companions or a low probability of BD formation due to reduced gas accretion rates during runaway accretion. However, the existence of this BD desert has not been firmly established for binaries with M dwarfs, which are the most abundant stellar population in the Galaxy, because of the limited sample size of BD binaries. Therefore, expanding the sample size of binary BD systems is crucial for gaining deeper insights into the intricacies of BD formation.

Microlensing, as it does not rely on the luminosity of lens objects, serves as an important tool for detecting binaries containing faint BD companions. To create a BD binary sample independent of the stellar types of primary stars, we extensively have examined microlensing data collected by high-cadence surveys since 2016. From this investigation, we reported six BD binaries detected during the 2016–2018 seasons (Han et al. 2022, Paper I), four binaries during the 2018–2020 seasons (Han et al. 2023a, Paper II), and another four binaries in the 2021 season (Han et al. 2023b, Paper III). The key parameter distinguishing a BD from a low-mass star at the upper mass bound

---

⋆ Corresponding author; `leecu@kasi.re.kr` and from large-mass planets at the lower mass bound is the mass. However, it is generally very difficult to determine the mass of a lens. Therefore, in selecting the BD sample, the previous three studies employed a method in which the mass ratio between a BD companion and its stellar host is less than $q_{\rm max} = 0.1$. This approach was chosen because the mass ratio between the lens components can be accurately measured for most binary-lens single-source (2L1S) lensing events, and companions with mass ratios less than $q_{\rm max}$ are highly likely to be BDs, considering that most lensing events are produced by low-mass stars (Han & Gould 2003).

Apart from the BDs documented in Papers I through III since 2016, specific BD detections were singled out for their own scientific significance. In the single-lens single-source (1L1S) lensing event OGLE-2017-BLG-0896, the lens was identified as an isolated BD based on the measured lens mass, determined through microlens-parallax analysis with additional data from the space-based *Spitzer* telescope (Shvartzvald et al. 2019). Extra *Spitzer* observations also revealed that the lenses of the events MOA-2016-BLG-231 (Chung et al. 2019) and OGLE-2019-BLG-0033 (Herald et al. 2022) were binaries consisting of BD companions and M-dwarf primaries. Additionally, the lens of OGLE-2016-BLG-1266 was found to be a binary composed of a BD and a super-Jupiter (Albrow et al. 2018). For OGLE-2017-BLG-1522, the lens was identified as a planetary system in which a BD primary hosts a giant planet companion (Jung et al. 2018). Similarly, the lens of MOA-2015-BLG-337 was found to be a planetary system with a host near the BD/planetary-mass boundary or a BD binary (Miyazaki et al. 2018). Gould et al. (2022) reported an isolated BD from the analysis of the short timescale 1L1S event KMT-2022-BLG-2397. Additionally, Han et al. (2020) reported that the lenses of the short timescale 1L1S events MOA-2017-BLG-147 and MOA-2017-BLG-241 are likely to be isolated BDs, while the lens of MOA-2019-BLG-256 is a binary system with both companions likely being BDs. Another microlensing binary composed of two BDs was identified by determining the lens mass from the measured angular Einstein radius and microlens parallax of the 2L1S event OGLE-2016-BLG-1469L (Han et al. 2017a). By measuring the ground-based microlens parallax, it was reported that the lenses of MOA-2019-BLG-008 (Bachelet et al. 2022), OGLE-2016-BLG-0693 (Ryu et al. 2017), and OGLE-2014-BLG-1112 (Han et al. 2017b) are binaries composed of a main-sequence dwarf star and a BD companion. The list of microlensing BDs in binaries detected before the 2016 season is detailed in Table 1 of Chung et al. (2019).

Building on the work presented in Papers I through III, we report six additional BDs in binary systems identified through a systematic inspection of microlensing events detected by the Korea Microlensing Telescope Network (KMTNet; Kim et al. 2016) survey during the 2022 and 2023 seasons. To create a homogeneous sample of BD companions for future statistical analyses of BD properties, we applied the same criteria used in the previous detections.

2. Procedure of event selection

Identifying BD companions in gravitational lensing events requires systematic analysis of anomalous lensing events. In a lensing event produced by a binary composed of a planet and its stellar host, the mass ratio between the lens components is typically less than 10^{-2}. In such cases, the planetary nature of the lens can be readily identified because the anomaly usually appears as a short-term perturbation on the smooth 1L1S lensing light curve of the primary lens (Mao & Paczyński 1991; Gould & Loeb 1992). In contrast, for 2L1S events with BD lens companions with mass ratios in the range of $10^{-2} \lesssim q \lesssim 10^{-1}$, anomalies can often be difficult to distinguish from those of 2L1S events with roughly equal lens mass components. Therefore, we analyze all lensing events exhibiting anomalies characteristic of 2L1S events, such as spikes resulting from the source crossing the lensing caustic formed by a binary lens, or bumps resulting from the source approaching the cusp of the caustic. Caustics are positions on the source plane where the lensing magnification of a point source becomes infinite. They form when the lens is composed of multiple objects, and thus caustic-related features in the lensing light curve indicate that the lens is likely to be binary. The total number of microlensing events detected from the KMTNet survey was 2803 in the 2022 season and 3162 in the 2023 season. Approximately 10% of these events display anomalies of various origins, with about half of those anomalous events showing clear deviations involving caustics.

Modeling the light curves of 2L1S events involves searching for lensing parameters that best fit the observed light curves. Describing a 2L1S light curve requires seven basic parameters. The first three parameters $(t_0, u_0, t_{\rm E})$ describe the lens-source approach, representing the time of the closest approach, the lens-source separation at that time (impact parameter), and the event timescale, respectively. The value of the impact parameter is scaled to the angular Einstein radius ($\theta_{\rm E}$) of the lens system, and the timescale is defined as the duration for the source to transit $\theta_{\rm E}$. Two additional parameters (s, q) define the binary lens: s denotes the projected separation (normalized to $\theta_{\rm E}$), and q represents the mass ratio between the lens components. The sixth parameter, α, denotes the source trajectory angle, defined as the angle between the source trajectory and the binary lens axis. The final parameter, ρ, is the ratio of the angular source radius θ_* to the Einstein radius ($\rho = \theta_*/\theta_{\rm E}$; normalized source radius), characterizing the deformation of the lensing light curve due to finite-source effects during caustic crossings and approaches.

The modeling was carried out according to the following procedure. First, we conducted searches for the binary parameters s and q using a grid approach, covering a wide range that encompasses various populations of lens companions, including planets, BDs, and stars. The grid search was conducted over the ranges $-1 \leq \log s < 1$ for the binary separation and $-5 \leq \log q < 1$ for the mass ratio. During this process, modeling was done with multiple starting α values, which are divided into 21 intervals over the range $0 \leq \alpha < 2\pi$. The remaining lensing parameters were optimized using a downhill method based on the Markov chain Monte Carlo (MCMC) algorithm, employing an adaptive step-size Gaussian sampler (Doran & Mueller 2004). In the second step, we inspected the χ^2 map in the plane of grid parameters and identified local minima. In the final step, we refined the individual local solutions by allowing all parameters to vary freely. We compared the χ^2 values of the individual local solutions and presented a global solution. If multiple local solutions exist and there is a significant degeneracy among them, we present all degenerate solutions and examine the underlying reasons for this degeneracy.

For events with long timescales and well-covered light curves, we additionally conducted modeling considering higher-order effects. We consider two such effects: microlens-parallax and lens-orbital effects. The microlens-parallax effect is caused by the Earth's orbital motion, which induces deviations in the relative lens-source motion from a rectilinear path (Gould 1992). The lens orbital motion effect arises from the orbital motion of the lens itself, which also causes deviations from the rectilinear

Table 1. Source coordinates, baseline magnitude, and I-band extinction.

Parameter	$(\mathrm{RA}, \mathrm{Dec})_{\mathrm{J2000}}$	(l, b)	I_{base}	A_I
KMT-2022-BLG-0412	(18:16:43.38, −26:36:00.29)	(5°.439, −4°.824)	18.63	0.78
KMT-2022-BLG-2286	(17:56:39.66, −28:51:17.71)	(1°.305, −2°.035)	19.90	2.10
KMT-2023-BLG-0201	(17:59:48.01, −30:29:59.89)	(0°.217, −3°.446)	15.54	1.36
KMT-2023-BLG-0601	(17:27:03.64, −29:28:13.30)	(−2°.631, 3°.126)	20.05	1.86
KMT-2023-BLG-1684	(17:35:25.77, −35:16:52.68)	(−6°.523, −1°.537)	20.38	5.41
KMT-2023-BLG-1743	(17:54:53.73, −33:10:50.99)	(−2°.632, −3°.879)	17.89	1.40

relative motion between the lens and the source (Albrow et al. 2000). Measuring the microlens parallax (π_{E}) by incorporating higher-order effects in the modeling is important, because it can further constrain the physical lens parameters of the lens mass and distance[1]. For computing finite-source magnifications, we employed the map-making method detailed in Dong et al. (2006). In this procedure, we took into account the limb-darkening effect arising from the surface brightness variation of the source star.

Among the analyzed 2L1S events, we selected candidate BD 2L1S events by applying the criterion that the mass ratio between the binary lens components lies in the range of $10^{-2} < q < 10^{-1}$. For short timescale events with $t_{\mathrm{E}} \lesssim 10$ days, we set the upper limit of the mass ratio at $q_{\mathrm{max}} = 0.2$. This higher threshold accounts for the fact that lens mass is proportional to the square of the timescale, making lower-mass lenses more likely to produce short timescale events. We note that this criterion has been consistently applied in Papers I through III for finding BD companions. Therefore, the BDs identified in this and previous works form a homogeneous sample, which is crucial for the statistical analysis of BD properties. From this selection criterion, we identified six candidate events including KMT-2022-BLG-0412, KMT-2022-BLG-2286, KMT-2023-BLG-0201, KMT-2023-BLG-0601, KMT-2023-BLG-1684, and KMT-2023-BLG-1743. These candidate BD events account for roughly 3% of the approximately 200 anomalous lensing events from the 2022 and 2023 seasons with analyzed light curves. However, this fraction does not represent the true proportion of binary lenses containing a BD, as the selection process for BD candidates is not automated and thus subject to human bias.

Table 1 presents the coordinates, baseline magnitude of source stars, and extinction values toward the field of the events. For the identified events, we checked whether they were also observed by other lensing surveys, specifically the Microlensing Observations in Astrophysics (MOA; Bond et al. 2001) and the Optical Gravitational Lensing Experiment (OGLE; Udalski et al. 2015). We found that the OGLE group observed KMT-2023-BLG-0201, while the MOA group observed KMT-2023-BLG-0201 and KMT-2023-BLG-1743. For these additionally observed events, we included the data in our analyses.

3. Observations and data

The KMTNet survey has been fully operational since 2016, following a one-year commissioning run in the 2015 season. The primary aim of the survey is to discover extrasolar planets through the observation of lensing events in stars positioned within the Galactic bulge field. The survey utilizes three identical telescopes specifically designed for high-cadence monitoring, aiming to detect planets with masses below that of Earth. To ensure continuous monitoring of lensing events, the KMTNet telescopes are strategically distributed across three countries in the Southern Hemisphere: the Cerro Tololo Inter-American Observatory in Chile (KMTC), the South African Astronomical Observatory in South Africa (KMTS), and the Siding Spring Observatory in Australia (KMTA). Each telescope features a 1.6-meter aperture and is equipped with a camera that offers a field of view spanning 4 square degrees. KMTNet observations primarily utilize the I passband, with approximately one-tenth of the images taken in the V band to measure the color of the source.

The MOA survey utilizes the 1.8-meter telescope at the Mt. John Observatory in New Zealand, while the OGLE survey utilizes the 1.3-meter telescope at the Las Campanas Observatory in Chile. These telescopes are equipped with cameras that provide fields of view of 1.4 and 2.2 square degrees, respectively. While OGLE observations were conducted in the same I band used by the KMTNet survey, observations by the MOA group were conducted in a customized MOA-R band.

Images from the surveys were reduced and photometry of the events was performed using the automated pipelines specific to each survey. The pipeline employed by the KMTNet survey was developed by Albrow et al. (2009), while those utilized by the OGLE and MOA groups were developed by Udalski (2003) and Bond et al. (2001), respectively. To utilize optimal data, we performed additional photometry on the KMTNet data using the code developed by Yang et al. (2024). During the modeling process, we adjusted the error bars of the data not only to normalize the χ^2 value for each data set to unity but also to ensure consistency between the error bars and the scatter of the data. This normalization process was done following the routine detailed in Yee et al. (2012).

4. Analyses of events

In this section, we present the analyses performed for the individual lensing events. For each event, we begin by describing the anomaly observed in the light curve, proceed to present the best-fit parameters, and conclude with a description of the lens system's configuration. In describing the light curve, we use an abridged Heliocentric Julian Date, defined as $\mathrm{HJD}' \equiv \mathrm{HJD} - 2450000$.

---

[1] None of the six events analyzed in this work showed detectable higher-order effects. Four of these events had timescales shorter than a month, which is insufficient to produce noticeable deviations. In one of the remaining events with a relatively long timescale, the photometric precision was insufficient to measure the subtle deviations caused by higher-order effects. In the other event, higher-order effects went undetected because the light curve was only partially observed.

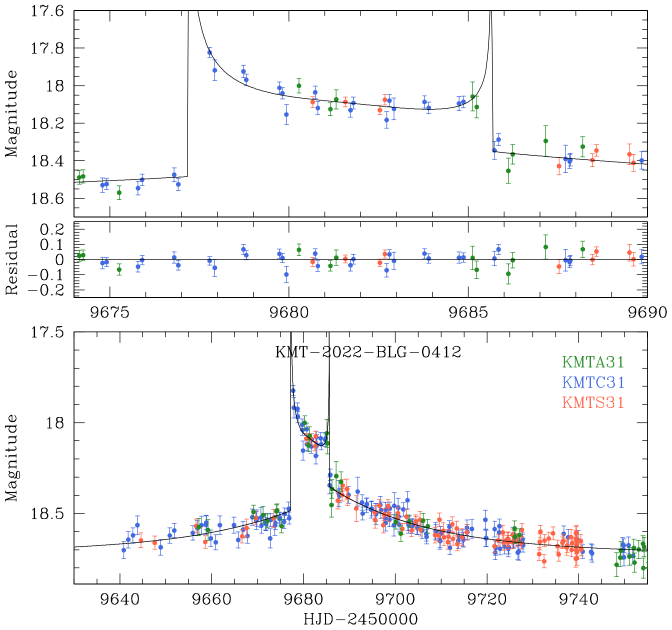

Fig. 1. Lensing light curve of KMT-2022-BLG-0412. The lower panel provides a comprehensive view, while the upper two panels offer magnified views around the caustic-crossing features and the residuals from the model. The curve overlaid on the data points is the best-fit model. The colors of the data points are selected to correspond to the telescope labels in the legend.

Table 2. Lensing parameters of KMT-2022-BLG-0412.

Parameter	Value
χ^2	496.5
t_0 (HJD′)	9683.289 ± 1.002
u_0	0.387 ± 0.030
t_E (days)	50.75 ± 2.14
s	0.9124 ± 0.0091
q	0.075 ± 0.017
α (rad)	2.694 ± 0.076
ρ (10^{-3})	<4

4.1. KMT-2022-BLG-0412

The lensing magnification of the source flux for the lensing event KMT-2022-BLG-0412 commenced prior to the onset of the 2022 bulge season on March 1, 2022. The gravitational lensing nature of the source flux variation was discerned on April 13 (HJD′ = 9683). This event was exclusively observed by the KMTNet group, with the source situated in the KMTNet BLG31 field, toward which observations were conducted at a cadence of 2.5 hours.

Figure 1 displays the light curve of the event. The light curve features two spikes, occurring at approximately HJD′ = 9677.2 and 9685.7, caused by caustic crossings of the source star. Because a caustic forms a closed curve, caustic spikes appear in pairs, with each pair arising when the source enters and exits the caustic. Between the caustic spikes, the light exhibits a skewed variation resembling a "U" shape. The left and right sides of the caustic feature are asymmetric, with the region just after the caustic exit being approximately 0.11 mag brighter than the region before the caustic entrance.

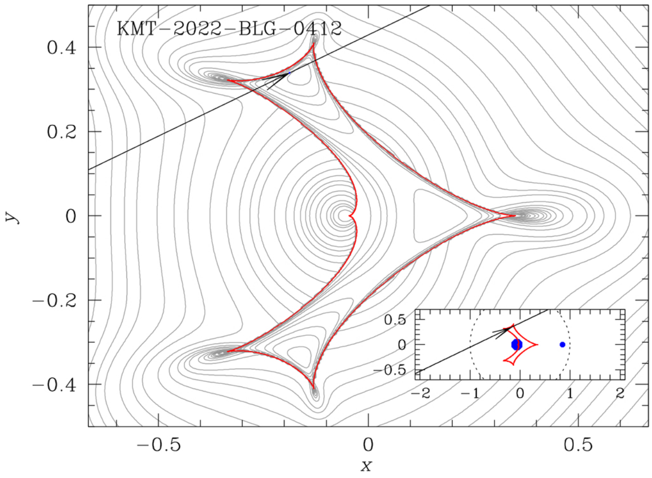

Fig. 2. Configuration of the lens system for the lensing event KMT-2022-BLG-0412. The red figure composed of concave curves represents the caustic, while the arrowed line represents the trajectory of the source. The grey curves encompassing the caustic represent equi-magnification contours. Lengths are scaled to the angular Einstein radius of the lens system. The inset shows the comprehensive view including the positions of the lens components (marked by blue dots) and Einstein radius (dotted circle).

From the modeling the observed light curve, we identified a unique solution. In Table 2, we present the lensing parameters of the solution along with the χ^2 value of the model fit. The model curve is depicted in Figure 1. The lower panel offers a comprehensive view, while the upper two panels provide magnified views of the caustic-crossing features and the residuals from the model. The limited coverage of both caustic spikes hindered the precise determination of the normalized source radius, resulting in only an upper limit being established. The parameters characterizing the binary lens are $(s, q) \sim (0.91, 0.075)$, indicating the presence of a low-mass companion with a projected separation slightly less than the Einstein radius. The timescale of the event, $t_E \sim 51$ days, is fairly long, constituting a sizable portion of the Earth's orbital period. However, determining the microlens parallax proved difficult, primarily due to substantial photometric uncertainties arising from the faintness of the source.

Figure 2 illustrates the lens-system configuration, showing the source's trajectory with respect to the caustic formed by the binary lens. The companion is positioned slightly inside the Einstein ring. Despite the low mass ratio, the lens companion generates a singular, expansive resonant caustic due to the binary separation's close proximity to unity. This caustic consists of six folds, with the two caustic spikes occurring as the source traversed the upper two folds that connect the central and outer regions of the caustic. The asymptotic approach of the source near the upper fold led to the skewed flux variation observed in the region between the caustic spikes.

4.2. KMT-2022-BLG-2286

The KMTNet group discovered the lensing-induced source flux magnification of the lensing event KMT-2022-BLG-2286 on October 4, 2022, which corresponds to HJD′ ∼ 9856. Figure 3 displays the light curve of the lensing event. Inspection of the light curve reveals two anomalous features: caustic-crossing feature with two spikes at HJD′ ∼ 9852.2 and 9856.4 and a weak bump at HJD′ ∼ 9858.1. The last observation of the season was done on October 21, HJD′ ∼ 9874.2. The event was very

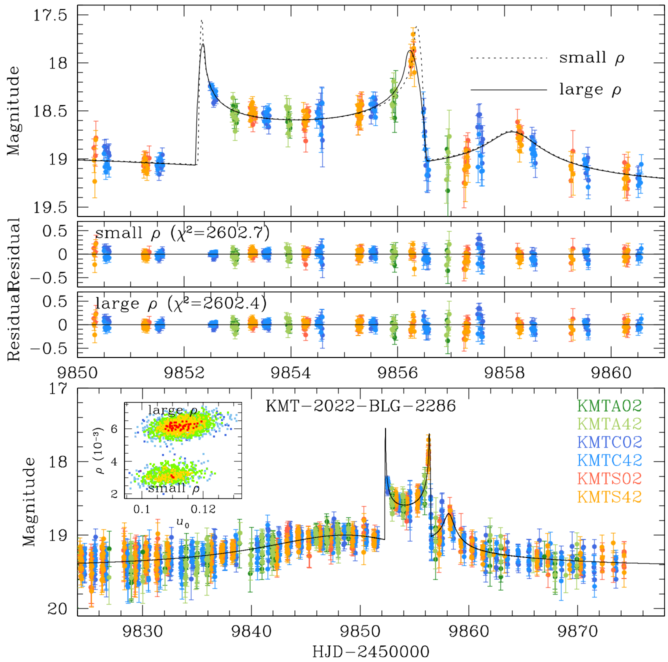

Fig. 3. Lensing light curve of KMT-2022-BLG-2286. The notations used are identical to those employed in Fig. 1. The inset in the bottom panel indicates the locations of the small-ρ and large-ρ solutions in the scatter plot of MCMC points on the u_0–ρ plane. The color scheme is set up to represent points as red ($\leq 1\sigma$), yellow ($\leq 2\sigma$), green ($\leq 3\sigma$), and cyan ($\leq 4\sigma$).

Table 3. Lensing parameters KMT-2022-BLG-2286.

Parameter	Small ρ	Large ρ
χ^2	2602.7	2602.4
t_0 (HJD′)	9854.695 ± 0.056	9854.7088 ± 0.056
u_0	0.1085 ± 0.0052	0.1120 ± 0.0052
t_E (days)	14.69 ± 0.34	14.70 ± 0.35
s	1.4036 ± 0.0060	1.4096 ± 0.0065
q	0.0896 ± 0.0063	0.0915 ± 0.0066
α (rad)	5.198 ± 0.016	5.205 ± 0.016
ρ (10^{-3})	3.12 ± 0.32	6.09 ± 0.49

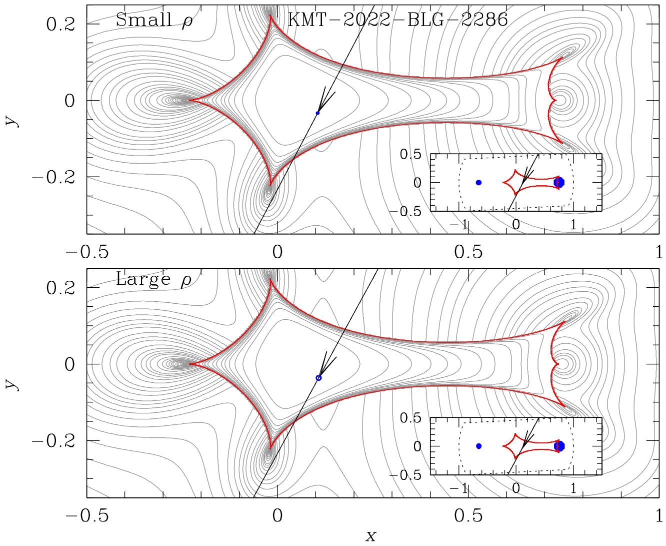

Fig. 4. Lens-system configuration of KMT-2022-BLG-2286. The upper and lower panels show configurations of the "small-ρ" and "large-ρ" solutions, respectively. In each panel, the small empty circle on the source trajectory indicates the scaled size of the source.

densely observed due to the source being located in the overlapping region of the two prime KMTNet fields, BLG02 and BLG42. Each field was observed with a 0.5-hour cadence, resulting in a combined cadence of 0.25 hours.

We have identified two solutions with nearly identical binary parameters, $(s, q) \sim (1.4, 0.09)$. Table 3 presents the full lensing parameters for both solutions. The primary disparity between them lies in the normalized source radius: $(3.12 \pm 0.32) \times 10^{-3}$ for one solution and $(6.09 \pm 0.49) \times 10^{-3}$ for the other, which we label as the "small-ρ" and "large-ρ" solutions, respectively. In the inset of the bottom panel of Figure 3, we present locations of the two local solutions in the scatter plot of points on the MCMC chain on the u_0–ρ parameter plane. The degeneracy between the two solutions is very severe, with the large-ρ solution preferred by only $\Delta\chi^2 = 0.3$. We conducted separate analyses for each solution due to discrepancies in the angular Einstein radii resulting from the differing normalized source radii. This distinction is crucial because θ_E serves as a critical observable constraining the physical properties of the lens. The two local solutions yield different values for the angular Einstein radius and the relative lens-source proper motion. Then, this degeneracy can be resolved by measuring the relative lens-source proper motion through future Adaptive Optic (AO) observations. The upper panels of Figure 3 display the model curves and residuals for the two degenerate solutions. While subtle distinctions are evident in the model light curve during the caustic exit, pinpointing a definitive solution proves challenging due to data uncertainties in this region.

Figure 4 illustrates the configurations of the lens systems corresponding to the two solutions. As expected, given the similarity in their lensing parameters, the configurations closely resemble each other. We denote the source size, scaled to the caustic size, as an empty circle on the source trajectory. In both solutions, the lens forms a single resonant caustic elongated along the binary axis, with the companion positioned on the left side in the map. The source traverses diagonally through the region between the primary and companion lens components of the caustic, resulting in the observation of two caustic spikes. The bump occurring at HJD′ ∼ 9858.1 corresponds to the moment when the source approaches the lower left cusp of the caustic.

4.3. KMT-2023-BLG-0201

The brightening of the source star in KMT-2023-BLG-0201 commenced early in the 2023 season, and the KMTNet survey identified the gravitational lensing nature of this light variation on March 29, 2023 (HJD′ ∼ 10013.2). The event was also observed by the OGLE and MOA groups, which labeled it OGLE-2023-BLG-0263 and MOA-2023-BLG-102, respectively. Following its detection, the event exhibited a sequence of anomalies, including a weak bump around HJD′ ∼ 10045, two distinct caustic spikes at HJD′ ∼ 10049.1 and HJD′ ∼ 10053.2, and another bump centered around HJD′ ∼ 10056. Figure 5 presents the light curve of the event, combining data from the three lensing surveys.

Modeling the light curve resulted in a unique solution with binary parameters of $(s, q) \sim (1.1, 0.20)$ and an event timescale of $t_E \sim 10$ days. Despite the mass ratio being higher than the basic threshold of $q_{\max} = 0.1$, the event was selected as a BD

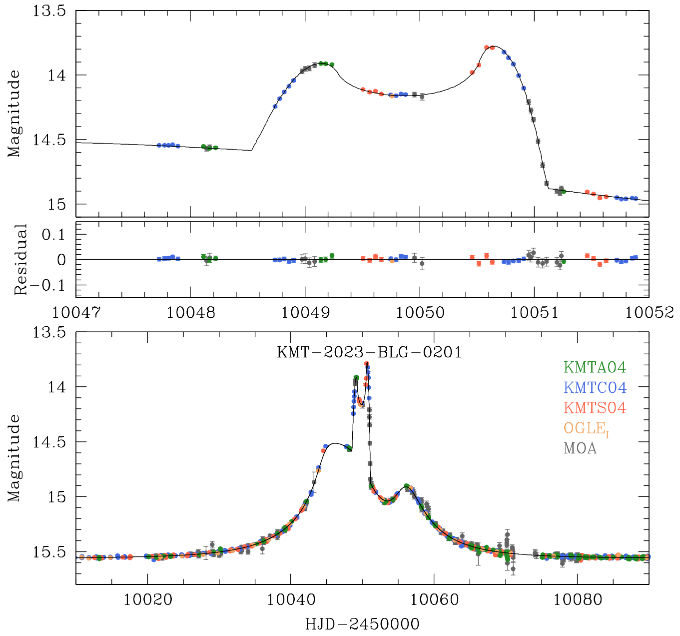

Fig. 5. Light curve of the lensing event KMT-2023-BLG-0201.

Table 4. Lensing parameters of KMT-2023-BLG-0201.

Parameter	Value
χ^2	1916.3
t_0 (HJD′)	10048.980 ± 0.011
u_0	0.3583 ± 0.0012
$t_{\rm E}$ (days)	9.995 ± 0.015
s	1.10201 ± 0.00058
q	0.2030 ± 0.0020
α (rad)	3.4596 ± 0.0012
ρ (10^{-3})	22.29 ± 0.19

candidate due to its short timescale. The full lensing parameters are detailed in Table 4. The caustic spikes exhibit pronounced finite source size effects, resulting in a rounded shape during caustic crossings. Both caustic-crossing segments of the light curve were densely resolved by the combined data sets, leading to a precisely measured normalized source radius of $\rho = (22.29 \pm 0.19) \times 10^{-3}$.

The lens-system configuration for the event is shown in Figure 6. As with the previous two events, the binary lens forms a resonant caustic. The source traversed the upper two folds of the caustic at an angle, resulting in the two observed caustic spikes. Before entering the caustic, the source approached the upper left cusp, generating the initial weak bump around HJD′ ∼ 10045. After exiting the caustic, it neared another cusp on the right side of the binary axis, causing a second bump around HJD′ ∼ 10056.

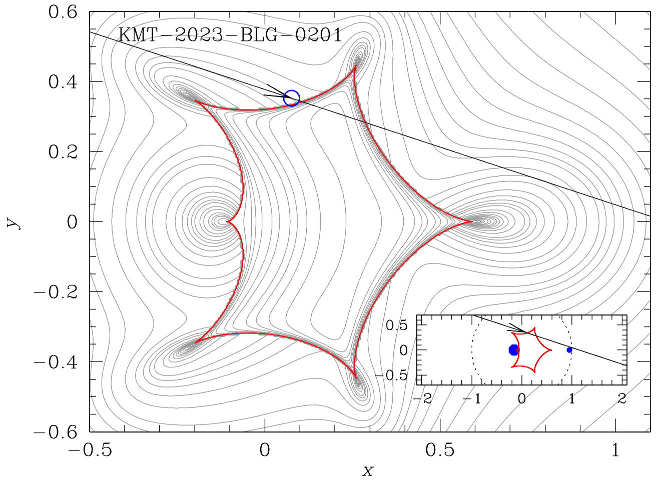

Fig. 6. Configuration of the lens system KMT-2023-BLG-0201.

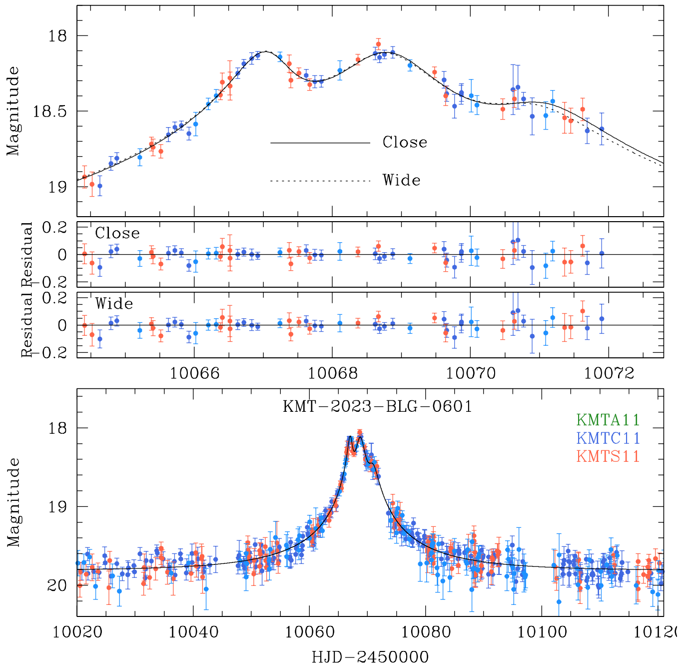

Fig. 7. Light curve of the lensing event KMT-2023-BLG-0601.

4.4. KMT-2023-BLG-0601

The lensing event KMT-2023-BLG-0601 was detected on April 28, 2023 (HJD′ ∼ 10063), about five days before its peak. It was exclusively observed by the KMTNet group with a cadence of 1.0 hour. Figure 7 presents the light curves constructed by combining data from the three KMTNet telescopes. The peak region of the light curve features three successive bumps, each separated by approximately two days. These bumps likely result from the source approaching close to the caustics near the primary lens. An anomaly consisting of three closely spaced bumps can occur when a caustic is skewed, with its cusps located on one side of the caustic produced by a binary lens. Such a skewed caustic can be formed by a binary lens with a small mass ratio between its components, as demonstrated in the cases of OGLE-2005-BLG-071Lb (Udalski et al. 2005) and KMT-2018-BLG-0885 (Han et al. 2023a).

Detailed modeling of the light curve resulted in two sets of solutions. The binary parameters for these solutions are $(s, q)_{\rm close} \sim (0.56, 0.064)$ and $(s, q)_{\rm wide} \sim (1.72, 0.067)$. The full lensing parameters for both solutions, along with their χ^2 values, are listed in Table 5. Figure 7 presents the model curves and residuals for the two solutions. The difference in χ^2 between them is very minor, $\Delta\chi^2 = 0.2$, indicating that the solutions are highly degenerate. The similarity between the model curves arises from the well-known close-wide degeneracy (Griest & Safizadeh 1998; Dominik 1999; An 2005), as shown

Table 5. Lensing parameters of KMT-2023-BLG-0601.

Parameter	Small ρ	Large ρ
χ^2	930.9	931.1
t_0 (HJD′)	10068.687 ± 0.036	10068.679 ± 0.039
u_0	0.0615 ± 0.0075	0.0638 ± 0.0059
t_E (days)	23.02 ± 2.93	23.24 ± 1.70
s	0.557 ± 0.013	1.719 ± 0.046
q	0.0643 ± 0.0078	0.0674 ± 0.0063
α (rad)	1.426 ± 0.016	1.42 ± 0.018
ρ (10^{-3})	–	–

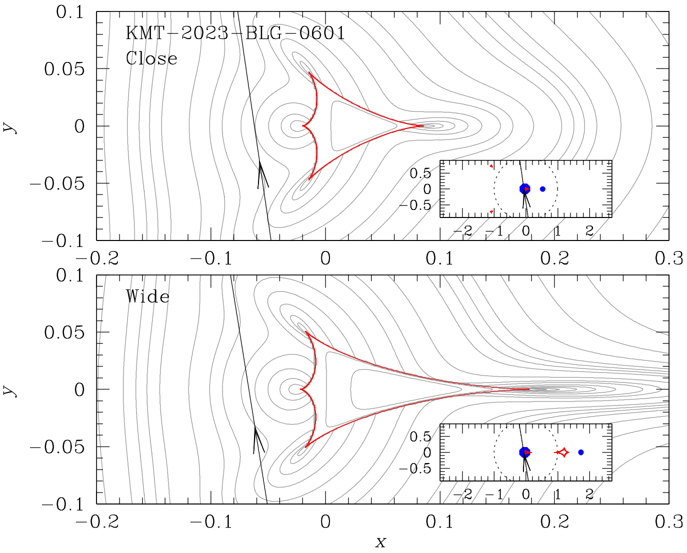

Fig. 8. Configuration of the lens system KMT-2023-BLG-0601.

by the binary separations being related by $s_{\text{close}} \sim 1/s_{\text{wide}}$ and their similar mass ratios.

Figure 8 displays the configurations of the lens system for the close (upper panel) and wide (lower panel) solutions. In both solutions, the source traverses the region behind the central caustic induced by a low-mass companion. As anticipated from the anomaly pattern, three of the four cusps of the central caustic are positioned on one side, resulting in the generation of weak bumps as the source approaches these cusps. In planetary lensing scenarios, a similar source trajectory would lead to an anomaly pattern where the middle bump is suppressed due to the relatively weaker middle cusp compared to the others (Han & Gaudi 2008). Consequently, planetary scenarios of the anomaly were excluded. The normalized source radius could not be determined because the separation between the source and caustic during the anomalies was too large to induce noticeable finite source effects.

4.5. KMT-2023-BLG-1684

The lensing-induced magnification of the source flux in the event KMT-2023-BLG-1684 commenced in the middle of the 2023 bulge season and persisted beyond its conclusion. Figure 9 illustrates the light curve of the event. The light curve was well characterized despite a relatively lower cadence (5 hours) and a very high extinction (A_I = 5 mag) toward the field. The KMTNet group detected the event early in its magnification phase on July 17, 2023 (HJD′ ~ 10143). The light curve peaked around HJD′ = 10198, during which it exhibited an anomaly characterized by a positive deviation lasting approximately three days. Another notable aspect of the anomaly is the significant disparity in lensing magnifications observed before and after the major anomaly.

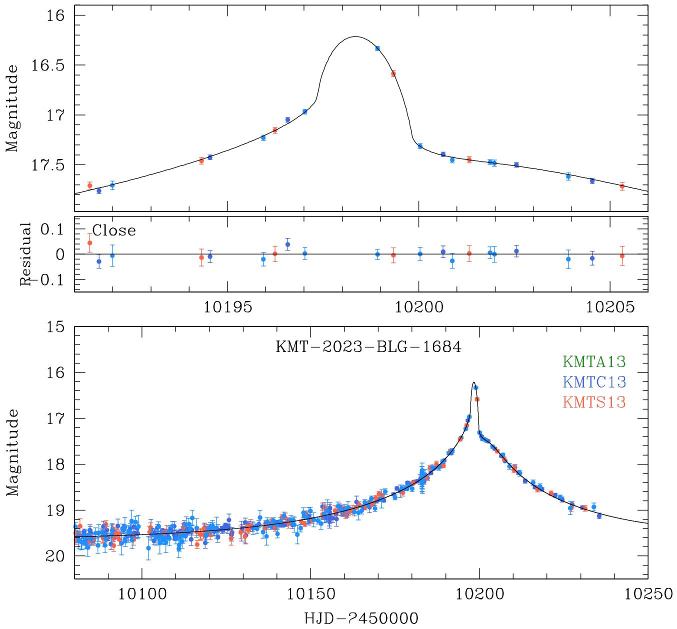

Fig. 9. Light curve of the lensing event KMT-2023-BLG-1684.

Table 6. Best-fit lensing parameters of KMT-2023-BLG-1684.

Parameter	Value
χ^2	679.9
t_0 (HJD′)	10199.300 ± 0.212
u_0	0.0995 ± 0.0067
t_E (days)	64.27 ± 2.97
s	0.693 ± 0.019
q	0.068 ± 0.010
α (rad)	0.534 ± 0.056
ρ (10^{-3})	18.4 ± 1.53

The analysis of the anomaly revealed a unique solution with binary parameters $(s, q) \sim (0.69, 0.068)$, indicating that the lens companion falls within the brown dwarf mass range. The full lensing parameters for this solution are listed in Table 6. The event's measured timescale, t_E ~ 64 days, is relatively long, prompting additional modeling to consider higher-order effects. However, accurately determining higher-order lensing parameters proved challenging, mainly because the declining part of the light curve had incomplete coverage. Nevertheless, the normalized source radius, $\rho = (18.4 \pm 1.53) \times 10^{-3}$, was precisely determined from the analysis of the anomaly, which was significantly influenced by finite source effects.

Figure 10 shows the arrangement of the source trajectory with respect to the caustic. The companion lying inside the Einstein ring induces two sets of caustics: one near the position of the primary and two peripheral caustics situated off the binary axis on the opposite side of the companion. The source crossed the lower tip of the central caustic, generating the anomaly near the peak of the light curve. The difference in magnifica-

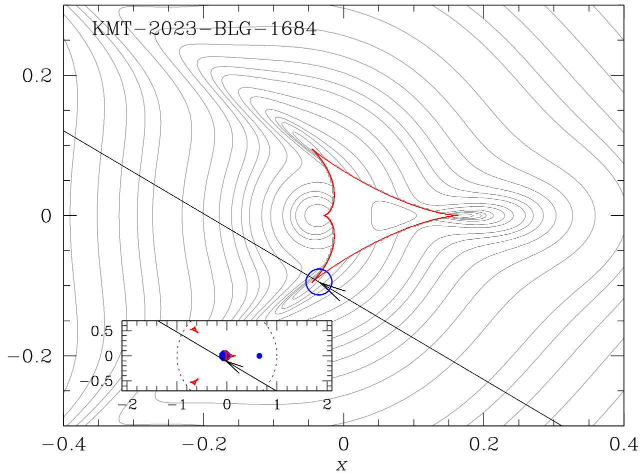

Fig. 10. Lens-system configuration of the lensing event KMT-2023-BLG-1684.

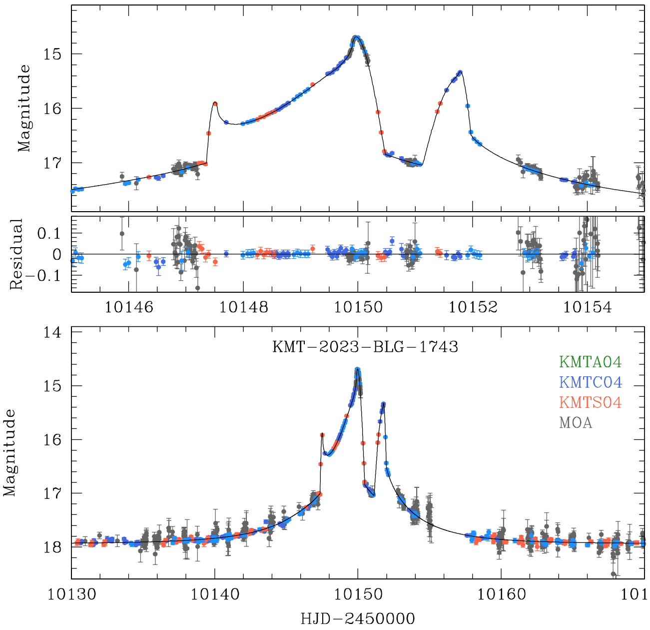

Fig. 11. Light curve of the lensing event KMT-2023-BLG-1743.

tion before and after crossing the caustic is attributed to negative magnification excess in the region behind the central caustic.

4.6. KMT-2023-BLG-1743

The KMTNet group initially detected the lensing event KMT-2023-BLG-1743 on July 19, 2023 (HJD′ ∼ 10145), and two days later, the MOA group confirmed it, designating it as MOA-2023-BLG-324. Figure 11 illustrates the light curve of the event, which exhibited two consecutive anomaly sets of caustic-crossing features. The first set displayed two distinct caustic peaks at HJD′ ∼ 10147.3 and HJD′ ∼ 10149.9, while the second set exhibited a single peak centered at HJD′ ∼ 10151.8. The asymmetric pattern between the caustic peaks of the first set suggests that the source approached a fold of the caustic asymptotically. The absence of a U-shaped pattern between the rising and falling parts of the latter anomaly set implies that the source crossed the tip of the caustic.

Table 7. Best-fit lensing parameters of KMT-2023-BLG-1743.

Parameter	Value
χ^2	2118.3
t_0 (HJD′)	60149.3030 ± 0.0099
u_0	−0.0023 ± 0.0016
$t_{\rm E}$ (days)	5.876 ± 0.049
s	1.0136 ± 0.0008
q	0.1770 ± 0.0031
α (rad)	5.2266 ± 0.0070
ρ (10^{-3})	14.49 ± 0.25

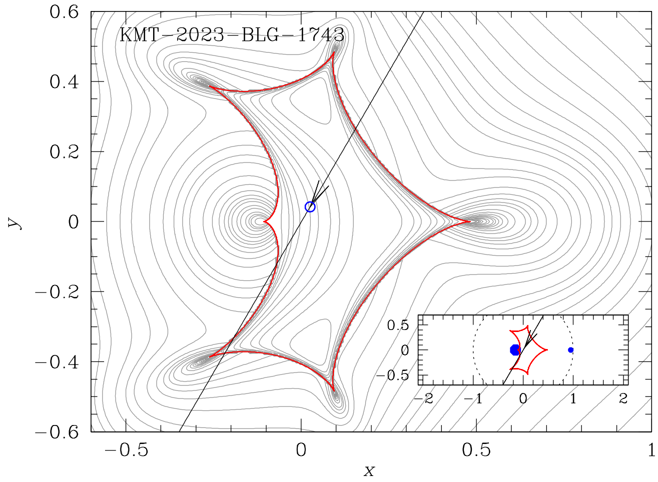

Fig. 12. Lens-system configuration of the event KMT-2023-BLG-1743.

The analysis of the light curve revealed a unique solution with binary parameters $(s, q) \sim (1.01, 0.18)$. Despite the mass ratio exceeding 0.1, the event was classified as a BD candidate due to its short timescale ($t_{\rm E} \sim 5.9$ days). All four caustic peaks were resolved using the combined data, leading to a precisely determined value of the normalized source radius $\rho = (14.49 \pm 0.25) \times 10^{-3}$. The complete lensing parameters are listed in Table 7.

Figure 12 illustrates the configuration of the lens system. The binary lens generated a resonant caustic composed of six folds. The source passed diagonally through the caustic, crossing these folds four times. Initially, the source entered the caustic by crossing the upper right fold and exited by traversing the lower left fold. This produced a classical caustic feature characterized by two spikes with a U-shaped trough region between them. The source then entered and exited the caustic again by moving through the area around the lower left cusp. The gap between this second entrance and exit was comparable to the size of the caustic, resulting in a single, merged anomaly feature.

5. Source stars and angular Einstein radii

In this section, we specify the source stars participating in the lensing events. Besides offering a detailed overview of each event, defining the source star is essential for calculating the angular Einstein radius using the relationship

$$\theta_{\rm E} = \frac{\theta_{\rm E}}{\rho}. \quad (1)$$

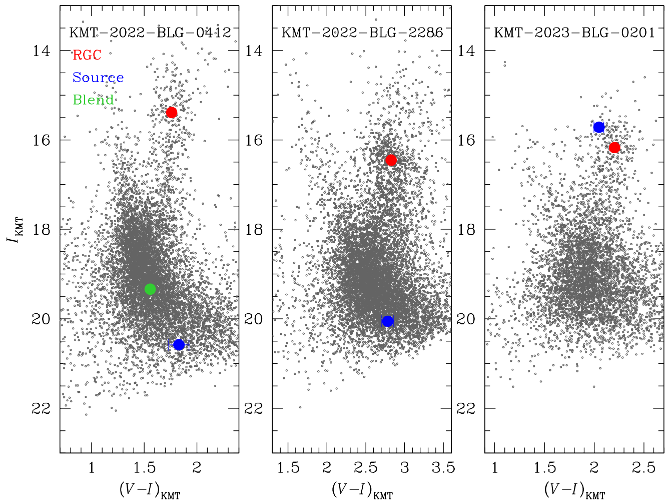

Fig. 13. Color-magnitude diagrams of source stars for the lensing event KMT-2022-BLG-0412, KMT-2022-BLG-2286, and KMT-2023-BLG-0201. In each panel, small filled dots marked in red and blue represent the positions of red giant clump (RGC) centroid and source, respectively. For the event KMT-2022-BLG-0412, we additionally mark the position of the blend.

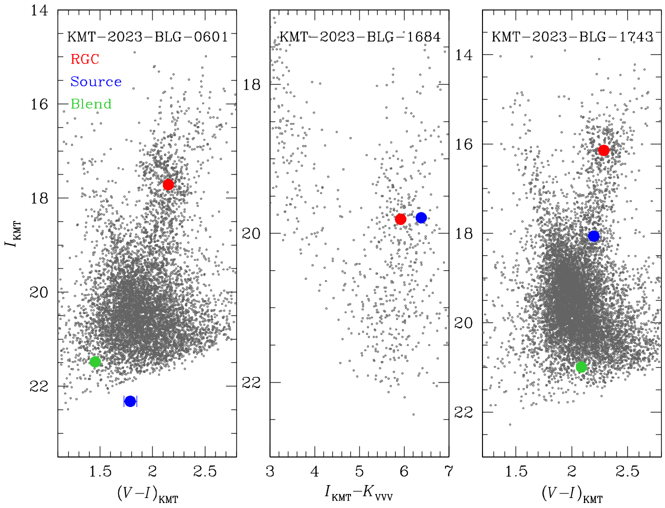

Fig. 14. Color-magnitude diagrams of source stars for the lensing event KMT-2023-BLG-0601, KMT-2023-BLG-1684, and KMT-2023-BLG-1743. Notations are same as those in Fig. 13. In the case of KMT-2023-BLG-1684, the color-magnitude diagram was compiled by aligning data from KMTNet observations with the VVV survey data.

The angular source radius, θ_*, is inferred from the source type, while the normalized source radius is determined through modeling.

The source is specified by assessing its color and brightness following the methodology outlined by Yoo et al. (2004). This method involves initially measuring the instrumental color and brightness of the source, which are then calibrated using the centroid of the red giant clump (RGC) in the color-magnitude diagram (CMD). The RGC centroid serves as a reference for this calibration due to its role as a standard candle, with its de-reddened color and magnitude for bulge stars well established in studies by Bensby et al. (2013) and Nataf et al. (2013).

In Figures 13 and 14, we present the source locations relative to the RGC centroids in the instrumental CMDs, constructed using KMTNet images processed with the pyDIA code (Albrow 2017). The instrumental source color and brightness, $(V-I, I)$, were determined by regressing the photometry data processed with the pyDIA code against the model. For events with measured blend colors, we also indicate the positions of the blends. For KMT-2023-BLG-1684, measuring the $V-I$ source color was challenging due to the severe extinction toward the field, with $A_I = 5.41$. In this case, we constructed $(I-K, I)$ CMD by matching KMT I-band pyDIA photometry to K-band VVV survey data (Minniti et al. 2017). The source magnitude from the fit, $I = 19.801 \pm 0.056$, is identical to the baseline magnitude, leading us to conclude that the source is unblended in the I band. Upon examining the nearest VVV entry, we found that the source is redder than the RGC centroid by $\Delta(I-K) = 0.46$.

With the measured instrumental color and magnitude, the de-reddened values were estimated as

$$(V-I, I)_0 = (V-I, I)_{\rm RGC,0} + \Delta(V-I, I), \tag{2}$$

where $(V-I, I)_{\rm RGC,0}$ represent the de-reddened values of the RGC centroid and $\Delta(V-I, I)$ denote the offset of the source from the RGC centroid. In Tables 8 and 9, we list the values of $(V-I, I)$, $(V-I, I)_{\rm RGC}$, $(V-I, I)_{\rm RGC,0}$, and $(V-I, I)_0$ together with the spectral types of the source stars. The source stars for KMT-2022-BLG-0412, KMT-2022-BLG-2286, and KMT-2023-BLG-0601 are main-sequence stars with spectral types K3.5, K3, and G2, respectively. On the other hand, the source stars for KMT-2023-BLG-0201, KMT-2023-BLG-1684, and KMT-2023-BLG-1743 are giant stars with spectral types K2, K7, and K3, respectively. For KMT-2023-BLG-1684, we first converted the measured color offset $\Delta(I-K)$ into $\Delta(V-I)$ using the color-color relation of Bessell & Brett (1988), and then estimated the de-reddened color $\Delta(V-I)_0$. We further verified the nature of the source by identifying its location in the $(J-K, I)$ CMD, which yielded a consistent result.

To estimate the angular source radius, we first converted the measured $V-I$ color to $V-K$ using the color-color relation from Bessell & Brett (1988). We then estimated θ_* using the relation between the angular source radius and $V-K$ color provided by Kervella et al. (2004). With the estimated value of θ_*, the angular Einstein radius was determined using the relation in Eq. (1). The relative lens-source proper motion was estimated from the measured angular Einstein radius and event timescale as

$$\mu = \frac{\theta_{\rm E}}{t_{\rm E}}. \tag{3}$$

In Table 10, we list the estimated values of θ_*, $\theta_{\rm E}$, and μ for the individual events. For KMT-2022-BLG-2286, which has two degenerate solutions with small and large ρ values, we present two sets of $(\theta_{\rm E}, \mu)$ values corresponding to each solution. For KMT-2022-BLG-0412, for which only the upper limit of ρ is constrained, we provide the lower limits of $\theta_{\rm E}$ and μ. In the case of KMT-2023-BLG-0601, the normalized source radius could not be measured, and thus $(\theta_{\rm E}, \mu)$ values are not presented.

6. Physical lens parameters

The physical parameters of a lens are constrained by the lensing observables $t_{\rm E}$ and $\theta_{\rm E}$. These observables are related to the lens parameters of the mass M and distance $D_{\rm L}$ by

$$t_{\rm E} = \frac{\theta_{\rm E}}{\mu}; \qquad \theta_{\rm E} = \sqrt{\kappa M \pi_{\rm rel}}, \tag{4}$$

where $\kappa = 4G/(c^2{\rm au})$, $\pi_{\rm rel} = {\rm au}(1/D_{\rm L} - 1/D_{\rm S})$ is the relative lens-source parallax, and $D_{\rm S}$ represents the distance to the source. In

Table 8. Source parameters of KMT-2033-BLG-0412, KMT-2022-BLG-2286, and KMT-2023-BLG-0201.

Quantity	KMT-2022-BLG-0412	KMT-2022-BLG-2286	KMT-2023-BLG-0201
$(V-I, I)$	$(1.830 \pm 0.096, 20.581 \pm 0.018)$	$(2.784 \pm 0.076, 20.055 \pm 0.015)$	$(2.049 \pm 0.049, 15.717 \pm 0.002)$
$(V-I, I)_{\rm RGC}$	$(1.761, 15.390)$	$(2.828, 16.455)$	$(2.205, 16.175)$
$(V-I, I)_{\rm RGC,0}$	$(1.060, 14.292)$	$(1.060, 14.389)$	$(1.060, 14.433)$
$(V-I, I)_0$	$(1.129 \pm 0.104, 19.483 \pm 0.027)$	$(1.016 \pm 0.086, 17.989 \pm 0.025)$	$(0.904 \pm 0.064, 13.975 \pm 0.020)$
Source type	K3.5V	K3V	K2III

Table 9. Source parameters of KMT-2023-BLG-0601, KMT-2023-BLG-1684, and KMT-2023-BLG-1743.

Quantity	KMT-2023-BLG-0601	KMT-2023-BLG-1684	KMT-2023-BLG-1743
$(V-I, I)$	$(1.789 \pm 0.061, 22.320 \pm 0.012)$	$(3.718 \pm 0.139, 19.801 \pm 0.056)$	$(2.198 \pm 0.003, 18.063 \pm 0.001)$
$(V-I, I)_{\rm RGC}$	$(2.151, 17.717)$	$(3.644, 20.045)$	$(2.287, 16.144)$
$(V-I, I)_{\rm RGC,0}$	$(1.060, 14.576)$	$(1.060, 14.620)$	$(1.060, 14.576)$
$(V-I, I)_0$	$(0.698 \pm 0.073, 19.179 \pm 0.023$	$(1.56 \pm 0.06, 14.375 \pm 0.056)$	$(0.971 \pm 0.040, 16.495 \pm 0.020)$
Source type	G2V	K7III	K3III

Table 10. Angular source radius, Einstein radius, and relative proper motion.

Event	θ_* (µas)	$\theta_{\rm E}$ (mas)	μ (mas/yr)
KMT-2022-BLG-0412	0.637 ± 0.080	>0.16	>1.15
KMT-2022-BLG-2286 (small ρ)	1.12 ± 0.13	0.361 ± 0.055	8.97 ± 0.14
(large ρ)	1.12 ± 0.13	0.185 ± 0.023	4.59 ± 0.56
KMT-2023-BLG-0201	6.33 ± 0.60	0.282 ± 0.027	10.30 ± 0.97
KMT-2023-BLG-0601	0.451 ± 0.046	–	–
KMT-2023-BLG-1684	9.13 ± 1.42	0.50 ± 0.09	2.82 ± 0.51
KMT-2023-BLG-1743	2.18 ± 0.18	0.157 ± 0.013	9.60 ± 0.79

a special case where an additional observable of the microlens parallax $\pi_{\rm E}$ is measured, the lens mass and distance are uniquely determined by the relations;

$$M = \frac{\theta_{\rm E}}{\kappa \pi_{\rm E}}; \qquad D_{\rm L} = \frac{\rm au}{\pi_{\rm E}\theta_{\rm E} + \pi_{\rm S}}\cdot \tag{5}$$

Here $\pi_{\rm S} = {\rm au}/D_{\rm S}$ represents the parallax of the source. The observables for the analyzed events were partially measured: the event timescale was determined for all events, but the angular Einstein radius was not measured for KMT-2022-BLG-0412 and KMT-2023-BLG-0601, and the microlens parallax could not be reliably determined for any of the events. Therefore, we estimate the physical lens parameters by conducting a Bayesian analysis using a prior Galaxy model along with the constraints provided by the measured observables of the events.

The Bayesian analysis was conducted as follows. Initially, we generated a large number of synthetic events through a Monte Carlo simulation. In this process, we determined the lens mass (M_i) from a model mass function and inferred the distances to the lens and source $(D_{{\rm L},i}, D_{{\rm S},i})$ as well as their relative proper motion (μ_u), using a Galaxy model. We employed the mass function model proposed by Jung et al. (2018) and the Galaxy model introduced by Jung et al. (2021). For each simulated event characterized by a set of the physical parameters $(M_i, D_{{\rm L},i}, D_{{\rm S},i}, \mu_i)$, we calculated the lensing observables of the timescale and angular Einstein radius by applying the equations in Eq. (4). In the subsequent step, we constructed the posterior distribution of the lens mass and distance by assigning a weight to each simulated event of

$$w_i = \exp\left(-\frac{\chi_i^2}{2}\right); \qquad \chi_i^2 = \frac{(t_{{\rm E},i} - t_{\rm E})^2}{\sigma(t_{\rm E})^2} + \frac{(\theta_{{\rm E},i} - \theta)^2}{\sigma(\theta)^2}\cdot \tag{6}$$

Here $(t_{\rm E}, \theta_{\rm E})$ denote the measured values of the lensing observables and $[\sigma(t_{\rm E}), \sigma(\theta_{\rm E})]$ represent their uncertainties.

Figures 15 and 16 display the Bayesian posteriors constructed for the companion lens mass and distance. For event KMT-2022-BLG-2286, which has two degenerate solutions with different $\theta_{\rm E}$ values, we provide two sets of posteriors. Table 11 summarizes the estimated masses of the primary lens (M_1) and its companion (M_2), along with the distance and the projected separation between M_1 and M_2 $(a_\perp)$. The projected separation is computed as $a_\perp = s D_{\rm L} \theta_{\rm E}$. The representative value is presented as the median of the posterior distribution, with the lower and upper limits estimated at the 16th and 84th percentiles, respectively.

An examination of the mass posteriors shows that the median masses of the lens companions for all events fall within the brown dwarf mass range of $13\,M_{\rm J} \leq M_2 \leq 80\,M_{\rm J}$. In terms of median posterior values, the mass of the primary lens ranges from $0.11\,M_\odot$ to $0.65\,M_\odot$, indicating that they are low-mass stars with substantially lower masses compared to the Sun. The table also provides the probabilities for the lens being in the disk, $p_{\rm disk}$, and in the bulge, $p_{\rm bulge}$. Specifically, for event KMT-2022-BLG-0412, the lens is more likely to be located in the disk. In contrast, for events KMT-2022-BLG-2286, KMT-2023-BLG-0201,

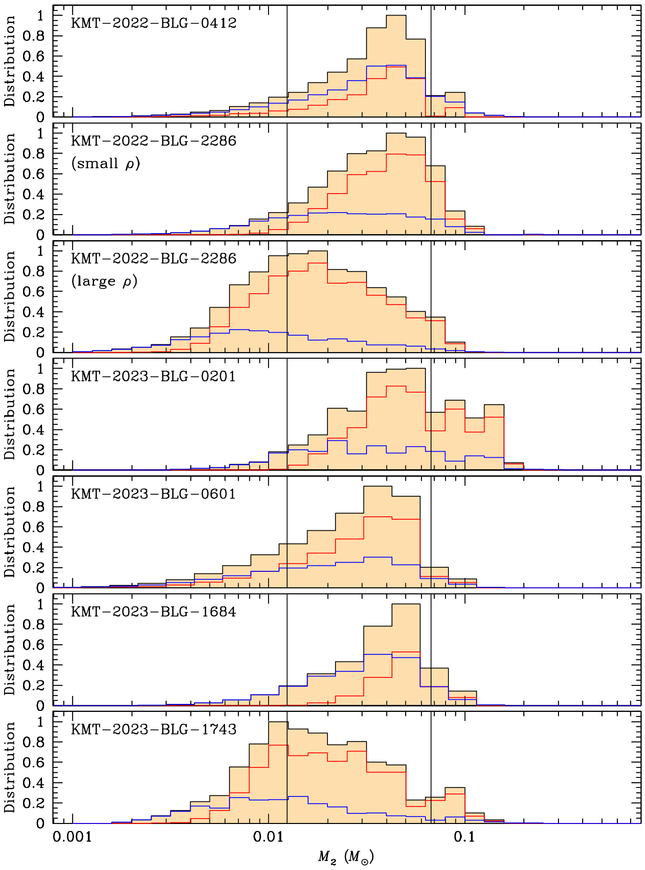

Fig. 15. Bayesian posteriors for the mass of the lens companion. For KMT-2022-BLG-2286, two posteriors corresponding to the "small ρ" and "large ρ" solutions are presented. The two vertical lines in each panel represent the BD mass range, which is set as 13 to 80 times of the Jupiter. The red and blue distributions represent the contributions from the disk and bulge lens populations, respectively, while the black curve represents the combined contributions of both populations.

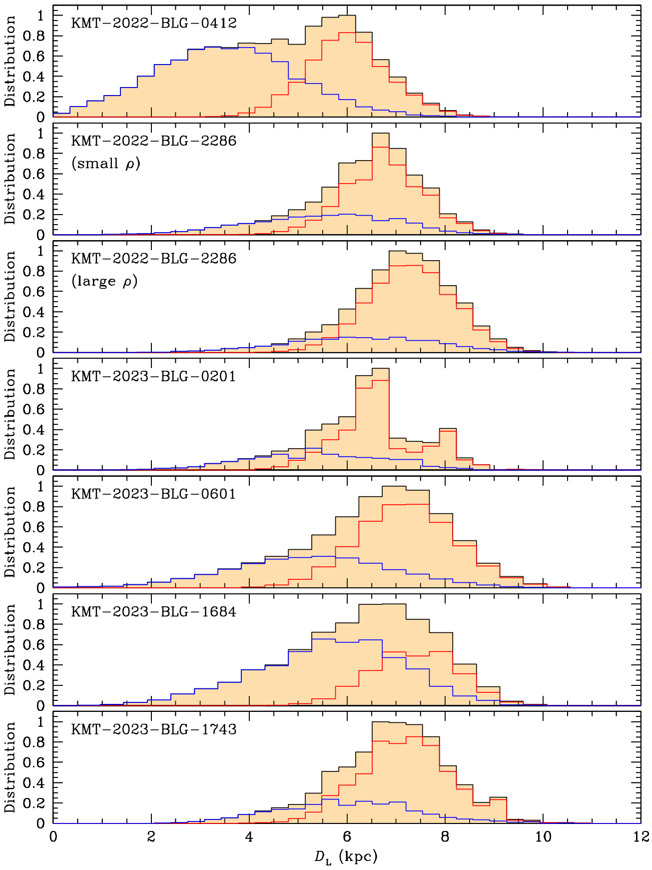

Fig. 16. Bayesian posteriors for the distance to the lens system. The notations are the same as those in Fig. 15.

KMT-2023-BLG-0601, and KMT-2023-BLG-1743, the lenses are more likely to be situated in the bulge. For event KMT-2023-BLG-1684, the probabilities of the lens being in the disk or the bulge are similar.

7. Summary and discussion

Building on the groundwork laid in Papers I through III, which aimed to construct a homogeneous sample of brown dwarfs in binary systems, we extended our investigation to microlensing events detected by the KMTNet survey during the 2022 and 2023 seasons. Due to the challenge of distinguishing brown dwarf events from those produced by binary lenses with nearly equal-mass components, we analyzed all lensing events detected during these seasons that exhibited anomalies characteristic of binary-lens systems. By applying the same criteria consistently used in previous studies, we identified seven additional brown dwarf candidates through the analysis of the following lensing events: KMT-2022-BLG-0412, KMT-2022-BLG-2286, KMT-2023-BLG-0201, KMT-2023-BLG-0601, KMT-2023-BLG-1684, and KMT-2023-BLG-1743.

Based on the Bayesian analysis performed with the constraints derived from measured lensing observables, it was determined that the median mass of the lens companions spans from 0.02 $M_\odot$ to 0.05 $M_\odot$, affirming their placement within the brown dwarf mass spectrum. Additionally, the mass range of the primary lenses extends from 0.11 $M_\odot$ to 0.65 $M_\odot$, suggesting that they are low-mass stars with significantly lesser masses compared to the Sun.

The BD nature of the lens companions can be verified through direct lens imaging from future high-resolution adaptive optics (AO) follow-up observations. This verification will be feasible once the lenses are sufficiently separated from the source stars. Around 2030, the AO observations with the 30-meter European Extremely Large Telescope are expected to resolve the lenses from the source stars. This will enable to estimate the mass of the primary lens. Combined with the accurately measured mass ratio, the BD nature of the lens companion can be confirmed.

Table 12 contains the necessary information for preparing these follow-up observations. This includes the expected separations between the lens and source in 2030 ($\Delta\theta_{2030}$), the K-band source magnitudes, and the values of the relative lens-source proper motion. The table covers events discussed in this work as well as those published in Papers I through III. Additionally, Gould et al. (2022) provided similar tables for over 100 planetary lensing events. Of these, 12 events have companion/primary mass ratios that meet our BD selection criterion ($10^{-2} < q < 10^{-1}$). Information on these events is included as well. For KMT-2023-BLG-0601, information on $\Delta\theta_{2030}$ is not presented because the value of the relative proper motion was not measured. In Figure 17, we plot the locations of the events in the plane of the K-band magnitude and $\Delta\theta_{2030}$. According to the table, the lens-

Table 11. Physical lens parameters.

Event	M_1 ($M_\odot$)	M_2 ($M_\odot$)	D_L (kpc)	$a_\perp$ (au)	$p_{\rm disk}$ (%)	$p_{\rm bulge}$ (%)
KMT-2022-BLG-0412	$0.65^{+0.38}_{-0.37}$	$0.040^{+0.023}_{-0.023}$	$4.82^{+1.63}_{-2.10}$	$2.86^{+0.97}_{-1.25}$	61	39
KMT-2022-BLG-2286 (small ρ)	$0.45^{+0.33}_{-0.24}$	$0.041^{+0.029}_{-0.022}$	$6.71^{+0.91}_{-1.33}$	$3.32^{+0.45}_{-0.66}$	33	67
(large ρ)	$0.20^{+0.29}_{-0.11}$	$0.018^{+0.026}_{-0.010}$	$7.32^{+0.97}_{-1.12}$	$2.02^{+0.27}_{-0.31}$	23	77
KMT-2023-BLG-0201	$0.26^{+0.30}_{-0.14}$	$0.052^{+0.061}_{-0.028}$	$6.55^{+1.13}_{-1.24}$	$2.05^{+0.35}_{-0.39}$	32	68
KMT-2023-BLG-0601	$0.51^{+0.40}_{-0.33}$	$0.033^{+0.026}_{-0.021}$	$6.95^{+1.27}_{-1.87}$	$1.56^{+0.29}_{-0.42}$	38	62
KMT-2023-BLG-1684	$0.68^{+0.34}_{-0.36}$	$0.046^{+0.023}_{-0.024}$	$6.66^{+1.36}_{-1.80}$	$2.48^{+0.50}_{-0.67}$	65	35
KMT-2023-BLG-1743	$0.11^{+0.16}_{-0.06}$	$0.019^{+0.029}_{-0.010}$	$7.13^{+1.05}_{-1.27}$	$1.16^{+0.17}_{-0.21}$	27	73

Table 12. Relative proper motion, angular separation in 2030, and K-band source magnitude.

	Event	μ (mas/yr)	$\Delta\theta_{2030}$ (mas)	K (mag)
Gould et al. (2022)	OGLE-2016-BLG-0596	5.1 ± 0.8	71.4	17.89
	OGLE-2016-BLG-0693	1.5 ± 0.2	21.0	18.64
	OGLE-2016-BLG-1190	1.9 ± 0.2	26.6	18.69
	KMT-2016-BLG-0212	8.1 ± 2.5	113.4	18.41
	KMT-2016-BLG-1107	2.6 ± 0.4	36.4	12.79
	KMT-2016-BLG-2605	12.3 ± 1.0	172.2	16.58
	OGLE-2017-BLG-1375	3.6 ± 0.5	46.8	19.28
	OGLE-2017-BLG-1522	3.2 ± 0.5	41.6	19.34
	OGLE-2018-BLG-1011	2.8 ± 0.2	33.6	16.65
	OGLE-2018-BLG-1647	0.6 ± 0.1	7.2	18.51
	OGLE-2019-BLG-0468	4.4 ± 0.6	48.4	18.73
	KMT-2019-BLG-0371	7.7 ± 0.7	84.7	17.17
Paper I	OGLE-2016-BLG-0890	6.30 ± 1.12	88.2	12.44
	MOA-2017-BLG-477	9.33 ± 0.83	121.29	18.21
	KMT-2018-BLG-0357	7.52 ± 1.05	90.24	17.81
	OGLE-2018-BLG-1489	4.89 ± 0.36	58.68	16.50
	OGLE-2018-BLG-0360	4.12 ± 0.59	49.44	16.83
Paper II	KMT-2018-BLG-0321	>2.4	>28.8	16.05
	KMT-2018-BLG-0885	>1.6	>19.2	18.58
	KMT-2019-BLG-0297	6.93 ± 0.51	76.23	17.88
	KMT-2019-BLG-0335	2.87 ± 1.16	31.57	18.89
Paper III	KMT-2021-BLG-0588	8.68 ± 0.80	78.12	17.68
	KMT-2021-BLG-1110	7.08 ± 0.62	63.72	18.75
	KMT-2021-BLG-1643	3.76 ± 0.58	33.84	19.51
	KMT-2021-BLG-1770	7.63 ± 0.90	68.67	17.08
This work	KMT-2022-BLG-0412	>1.1	>8.8	18.12
	KMT-2022-BLG-2286 (small ρ)	8.97 ± 0.14	71.7	16.93
	(large ρ)	4.59 ± 0.56	36.7	16.93
	KMT-2023-BLG-0201	10.30 ± 0.97	72.1	12.97
	KMT-2023-BLG-1684	2.82 ± 0.51	19.7	13.31
	KMT-2023-BLG-1743	9.60 ± 0.79	67.2	15.40

source separation will exceed 50 mas for KMT-2023-BLG-0201 and KMT-2023-BLG-1743, indicating that the lenses can be readily resolved with AO observations. In contrast, the expected separation for KMT-2023-BLG-1684, $\Delta\theta_{2030} \sim 20$ mas, is substantially smaller, suggesting difficulty in resolving the lens. For KMT-2022-BLG-2286, the expected separations for the small-ρ solution ($\Delta\theta_{2030} \sim 72$ mas) and the large-ρ solution ($\Delta\theta_{2030} \sim 37$ mas) differ significantly, indicating that AO follow-up will not only easily resolve the degeneracy but also yield a host-mass measurement.

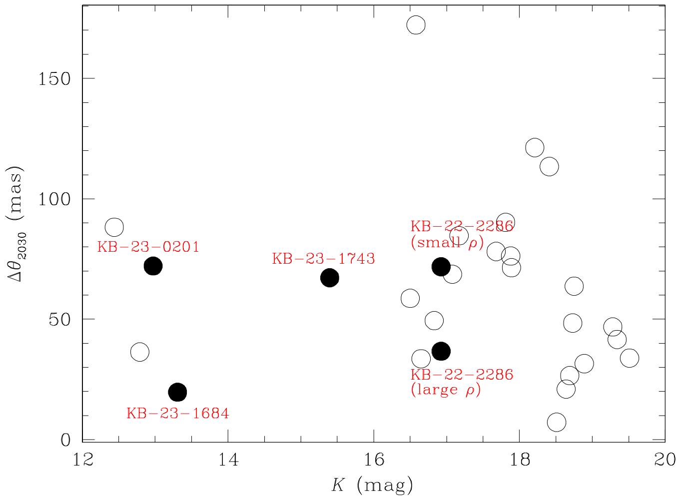

Fig. 17. BD candidate events in the plane of the K-band magnitude and $\Delta\theta_{2030}$. The events analyzed in this work are marked by filled dots.

Acknowledgements. Work by C.H. was supported by the grants of National Research Foundation of Korea (2019R1A2C2085965). J.C.Y. and I.-G.S. acknowledge support from U.S. NSF Grant No. AST-2108414. Y.S. acknowledges support from BSF Grant No. 2020740. This research has made use of the KMTNet system operated by the Korea Astronomy and Space Science Institute (KASI) at three host sites of CTIO in Chile, SAAO in South Africa, and SSO in Australia. Data transfer from the host site to KASI was supported by the Korea Research Environment Open NETwork (KREONET). This research was supported by KASI under the R&D program (Project No. 2024-1-832-01) supervised by the Ministry of Science and ICT. W.Z. and H.Y. acknowledge support by the National Natural Science Foundation of China (Grant No. 12133005). W. Zang acknowledges the support from the Harvard-Smithsonian Center for Astrophysics through the CfA Fellowship. The MOA project is supported by JSPS KAKENHI Grant Number JP24253004, JP26247023,JP16H06287 and JP22H00153.

References

Albrow, M. 2017, `https://doi.org/10.5281/zenodo.268049`
Albrow, M. D., Beaulieu, J.-P., Caldwell, J. A. R., et al. 2000, ApJ, 534, 894
Albrow, M., Horne, K., Bramich, D. M., et al. 2009, MNRAS, 397, 2099
Albrow, M. D., Yee, J. C., & Udalski, A. 2018, ApJ, 858, 107
An, J. H. 2005, MNRAS, 356, 1409
Bachelet, E., Tsapras, Y., Gould, A., et al. 2022, AJ, 164, 75
Bensby, T., Yee, J. C., Feltzing, S., et al. 2013, A&A, 549, A147
Bessell, M. S., & Brett, J. M. 1988, PASP, 100, 1134
Bond, I. A., Abe, F., Dodd, R. J., et al. 2001, MNRAS, 327, 868
Burrows, A., Marley, M., Hubbard, W. B., et al. 1997, ApJ, 491, 856
Chung, S.-J., Gould, A., Skowron, J., et al. 2019, ApJ, 871, 179
Chabrier, G., & Baraffe, I. 2000, ARA&A, 38, 337
Dominik, M. 1999, A&A, 349, 108
Dong, S., DePoy, D. L., Gaudi, B. S., et al. 2006, ApJ, 642, 842
Doran, M., & Mueller, C. M. 2004, JCAP, 09, 003
Gould, A. 1992, ApJ, 392, 442
Gould, A., & Loeb, A. 1992, ApJ, 396, 104
Gould, A., Jung, Y. K., Hwang, K.-H., et al. 2022, JKAS, 55, 173
Grether, D., & Lineweaver, C. H. 2006, ApJ, 640, 1051
Griest, K., & Safizadeh, N. 1998, ApJ, 500, 37
Han, C., & Gaudi, B. S. 2008, ApJ, 689, 53
Han, C., & Gould, A. 2003, ApJ, 592, 172
Han, C., Udalski, A., Sumi, T., et al. 2017a, ApJ, 843, 59
Han, C., Udalski, A., Bozza, V., et al. 2017b, ApJ, 843, 87
Han, C., Lee, C.-U., Udalski, A., et al. 2020, AJ, 159, 134
Han, C., Ryu, Y.-H., Shin, I.-G., et al. 2022, A&A, 667, A64
Han, C., Jung, Y. K., Kim, D., et al. 2023a, A&A, 675, A71
Han, C., Jung, Y. K., Bond, I. A., et al. 2023b, A&A, 678, A190
Herald, A., Udalski, A., Bozza, A., et al. 2022, A&A, 663, A100
Jung, Y. K., Udalski, A., Gould, A., et al. 2018, AJ, 155, 219
Jung, Y. K., Han, C., Udalski, A., et al. 2021, AJ, 161, 293
Kervella, P., Thévenin, F., Di Folco, E., & Ségransan, D. 2004, A&A, 426, 29
Kim, S.-L., Lee, C.-U., Park, B.-G., et al. 2016, JKAS, 49, 37
Mao, S., & Paczyński, B. 1991, ApJ, 374, L37
Marcy, G. W., & Butler, P. R. 2000, PASP, 112, 137
Minniti, D., Lucas, P., & VVV Team 2017, VizieR Online Data Catalog: II/348
Miyazaki, S., Sumi, T., Bennett, D. P., et al. 2018, AJ, 156, 136
Nataf, D. M., Gould, A., Fouqué, P., et al. 2013, ApJ, 769, 88
Ryu, Y.-H., Udalski, A., Yee, J. C., et al. 2017, AJ, 154, 247
Shvartzvald, Y., Yee, J. C., Skowron, J., et al. 2019, AJ, 157, 106
Udalski, A. 2003, Acta Astron., 53, 291
Udalski, A., Jaroszyński, M., Paczyński, B., et al. 2005, ApJ, 628, L109
Udalski, A., Szymański, M. K., Szymański, G., et al. 2015, Acta Astron., 65, 1
Yang, H., Yee, J. C., Hwang, K.-H., et al. 2024, MNRAS, 528, 11
Yee, J. C., Shvartzvald, Y., Gal-Yam, A., et al. 2012, ApJ, 755, 102
Yoo, J., DePoy, D. L., Gal-Yam, A., et al. 2004, ApJ, 603, 139

---

[1] Department of Physics, Chungbuk National University, Cheongju 28644, Republic of Korea
[2] Institute of Natural and Mathematical Science, Massey University, Auckland 0745, New Zealand
[3] Astronomical Observatory, University of Warsaw, Al. Ujazdowskie 4, 00-478 Warszawa, Poland
[4] Korea Astronomy and Space Science Institute, Daejon 34055, Republic of Korea
[5] Max Planck Institute for Astronomy, Königstuhl 17, D-69117 Heidelberg, Germany
[6] Department of Astronomy, The Ohio State University, 140 W. 18th Ave., Columbus, OH 43210, USA
[7] University of Canterbury, Department of Physics and Astronomy, Private Bag 4800, Christchurch 8020, New Zealand
[8] Department of Particle Physics and Astrophysics, Weizmann Institute of Science, Rehovot 76100, Israel
[9] Center for Astrophysics | Harvard & Smithsonian 60 Garden St., Cambridge, MA 02138, USA
[10] Department of Astronomy and Tsinghua Centre for Astrophysics, Tsinghua University, Beijing 100084, China
[11] School of Space Research, Kyung Hee University, Yongin, Kyeonggi 17104, Republic of Korea
[12] Institute for Space-Earth Environmental Research, Nagoya University, Nagoya 464-8601, Japan
[13] Department of Earth and Space Science, Graduate School of Science, Osaka University, Toyonaka, Osaka 560-0043, Japan
[14] Code 667, NASA Goddard Space Flight Center, Greenbelt, MD 20771, USA
[15] Department of Astronomy, University of Maryland, College Park, MD 20742, USA
[16] Department of Earth and Planetary Science, Graduate School of Science, The University of Tokyo, 7-3-1 Hongo, Bunkyo-ku, Tokyo 113-0033, Japan
[17] Instituto de Astrofísica de Canarias, Vía Láctea s/n, E-38205 La Laguna, Tenerife, Spain
[18] Institute of Astronomy, Graduate School of Science, The University of Tokyo, 2-21-1 Osawa, Mitaka, Tokyo 181-0015, Japan
[19] Oak Ridge Associated Universities, Oak Ridge, TN 37830, USA
[20] Institute of Space and Astronautical Science, Japan Aerospace Exploration Agency, 3-1-1 Yoshinodai, Chuo, Sagamihara, Kanagawa 252-5210, Japan
[21] Sorbonne Université, CNRS, UMR 7095, Institut d'Astrophysique de Paris, 98 bis bd Arago, 75014 Paris, France
[22] Department of Physics, University of Auckland, Private Bag 92019, Auckland, New Zealand
[23] University of Canterbury Mt. John Observatory, P.O. Box 56, Lake Tekapo 8770, New Zealand
[24] Department of Physics, University of Warwick, Gibbet Hill Road, Coventry CV4 7AL, UK
[25] Villanova University, Department of Astrophysics and Planetary Sciences, 800 Lancaster Ave., Villanova, PA 19085, USA